ROYAL SOCIETY
OF CHEMISTRY

PAPER

Check for updates

High-stability pillar-layered Zn/ZnCd-MOFs with optimized pores for efficient methane purification

Ya-Nan Guo,[a] Xiao-Yan Zhu,[a] Zi-Qian Zhou,[a] Liang Song,[a] Xiao-Hong Xiong,[b] Huan-Huan Sun,[a] Cheng-Xia Chen,[a] Ji-Jun Jiang, [ID][a] Dieter Fenske,[ac] Hong-Yan Chen, [ID][a] Zhang-Wen Wei [ID] *[a] and Cheng-Yong Su [ID] *[a]

Efficient methane (CH_4) purification is critical for the full utilization of clean natural gas in the petrochemical industry. Compared with conventional energy-intensive low-temperature distillation, adsorptive separation using porous metal–organic frameworks (MOFs) represents a more energy-efficient and high-performance alternative. Herein, we synthesized a series of layer-based Zn- and Zn/Cd-MOFs (LIFM-260–265) by regulating metal nodes and pillar ligands of different sizes to tailor their topologies and pore dimensions. Of these materials, the porous MOFs with pillar-layer structures (LIFM-263–265) enable simultaneous removal of ethane (C_2H_6) and propane (C_3H_8) from a $CH_4/C_2H_6/C_3H_8$ ternary mixture. Among them, LIFM-265 delivers the highest productivity of high-purity (>99.8%) CH_4 (7.92 mmol g^{-1}) based on single breakthrough curve tests, outperforming its analogues LIFM-263 and LIFM-264. Theoretical simulations reveal that the optimal pore structures and aromatic surface environments of LIFM-263–265 promote favorable interactions with C_2H_6 and C_3H_8 molecules, thus enhancing selective adsorption of C_2/C_3 hydrocarbons. This work provides valuable insights for the rational design of pillar-layered MOFs for methane purification.

1. Introduction

The main component of natural gas is methane (CH_4), which has a high energy density (55.7 MJ kg^{-1}) and low carbon dioxide emissions.[1] It is widely recognized that natural gas primarily consists of CH_4 (75–90%), C_2H_6 (0–20%), and C_3H_8 (0.01–5%), along with trace amounts of impurities such as H_2S, CO_2, N_2, and water vapor.[2] Methane purification not only produces high-purity methane for industrial production and combustion applications but also recovers high-value ethane (C_2H_6) and propane (C_3H_8).[3] Thus, it is of great significance to remove trace C_2H_6 and C_3H_8 from natural gas.[4]

Currently, the industrial separation of mixed light hydrocarbons is primarily achieved through cryogenic distillation, often involving high energy consumption, expensive equipment, and harsh operating conditions.[5,6] Therefore, there is a compelling need to explore an economical, efficient, and mild separation technology.[7] The adsorption and separation technology based on porous adsorbents has attracted extensive attention due to its low energy consumption. Some traditional porous materials, such as activated carbon, zeolite, and clay have been developed for gas adsorption and separation.[8–11] However, the adsorption capacity and separation selectivity of these adsorbents are not entirely satisfactory due to their limited pore space and uncontrollable pore surface functionality. Therefore, to meet the complex requirements of separation tasks, it is highly necessary to develop novel adsorbents that possess customizable structures and tunable surface properties for more efficient and environmentally friendly separation processes.[12]

Metal–organic frameworks (MOFs), as a class of porous materials, have shown significant potential in gas separation and purification, catalysis, drug delivery, and optical/electronic applications.[13–17] These advantages stem from their well-organized pore structures, large surface areas, structural tunabilities, and pore space functionalities.[18–21] A variety of MOFs, such as UiO-66,[22] Fe-MOF-74,[23] DMOF,[24] and MIL-101,[25] have been employed for methane purification. Among them, the simple, controllable pillar-layered MOF strategy, where planar layers are vertically connected *via* auxiliary ligands to form well-defined pillar-layered structures, has been proven to be an effective strategy to synthesize MOFs for light hydrocarbon separation.[26–29] Notably, heterometallic secondary building units (SBUs) and stability enhancement for pillar-layer MOFs still require further research. To develop new SBUs, Hong, Chen

[a]MOE Laboratory of Bioinorganic and Synthetic Chemistry, GBRCE for Functional Molecular Engineering, LIFM, IGCME, School of Chemistry, Sun Yat-Sen University, Guangzhou 510006, China. E-mail: cesscy@mail.sysu.edu.cn; weizhw3@mail.sysu.edu.cn

[b]Department of Chemistry and Chemical Engineering, Key Laboratory for Preparation and Application of Ordered Structural Materials of Guangdong Province, Shantou University, Shantou, 515063, China

[c]Institute of Nanotechnology (INT), Karlsruhe Nano Micro Facility (KNMF), Karlsruhe Institute of Technology (KIT), 76344 Eggenstein-Leopoldshafen, Germany

et al. selected Zn and Cd ions (different sizes but similar coordination properties) as metal nodes, and rigid, directionally favorable 1,3,5-tris(4-carboxyphenyl)benzene (H$_3$BTB) as the organic ligand.[30] They constructed a novel 2-dimensional (2D) bilayer structure based on a heterometallic Zn$_2$/Cd hourglass-shaped cluster (FJI-H16), and further introduced pillar ligands with varying sizes and flexibility (4,4′-bipyridine, BPY; *trans*-1,2-bis(4-pyridyl)ethane, BPE) to expand it into two new 3D frameworks (FJI-H17 and FJI-H18). These 3D frameworks allow tuning of pore size and flexibility, while exhibiting adjustable selective adsorption performance. Instead of traditional ditopic ligand, Cen, Li, Zhou *et al.* constructed a 2D layered structure using a tetrotopic ligand (tetra(4-carboxyphenyl)ethylene, H$_4$TCPE) and Zn^{2+}, which was further connected by linear BPY pillars to form a 2-fold interpenetrated 3D pillar-layered MOF (Zn-L$_{C-C}$) with enhanced stability.[31] They then substituted BPY with three unsaturated functional group-elongated ligands to synthesize a series of pillar-layer MOFs, improving the materials' porosity, specific surface area, adsorption capacity, and selectivity for C$_2$H$_2$. Wang *et al.* designed two interpenetrating pillar-layered MOFs (M-PTTB-BPY, M = Zn, Co) for efficient C$_2$H$_6$/C$_2$H$_4$ separation. The H$_4$PTTB ligand (4,4′,4″,4‴-(pyrazine-2,3,5,6-tetrayl)tetrabenzoic acid) and M$_2$-paddlewheel nodes form 2D layers, while BPY pillars control the interlayer spacing.[32] By modifying the metal components, the interpenetration and pore properties of M-PTTB-BPY were fine-tuned, establishing

a correlation with its effectiveness in adsorptive separation of C$_2$H$_6$/C$_2$H$_4$. These excellent studies have demonstrated the effectiveness of the pillar-layered MOF strategy and the impact of high-connectivity ligands, pillar regulation, and metal type modification on MOF structures and properties, which inspires our work to construct novel pillar-layered MOFs using tritopic ligands, tunable pillars, heterometallic Zn/Cd nodes, and interpenetrated frameworks.

In this work, we synthesized a series of layer-based MOFs (LIFM-260 to LIFM-265; LIFM stands for Lehn Institute of Functional Materials) with structures evolving from 2D nonporous networks to 3D porous pillar-layer frameworks. These MOFs, constructed from a methyl-modified ligand, 1,3,5-tris(4-carboxyphenyl)benzene (H$_3$BTB-Me), and Zn/Cd metal nodes, demonstrate systematic structural progression through heterometallic doping and pillar ligand insertion, enabling precise control over dimensionality, topology, and porosity, with the aim of enhancing their adsorption and separation performance for simulated natural gas (C$_3$H$_8$/C$_2$H$_6$/CH$_4$ mixtures) (Fig. 1). Single-component gas adsorption tests revealed that the three pillar-layer MOFs, LIFM-263–265, exhibited higher adsorption capacities for C$_3$H$_8$ and C$_2$H$_6$, while showing a lower adsorption capacity for CH$_4$. Through isosteric heat of adsorption analysis, it is found that the interactions between C$_3$H$_8$/C$_2$H$_6$ and MOFs are stronger than those with CH$_4$. Among them, LIFM-265 displayed the highest C$_3$H$_8$/CH$_4$
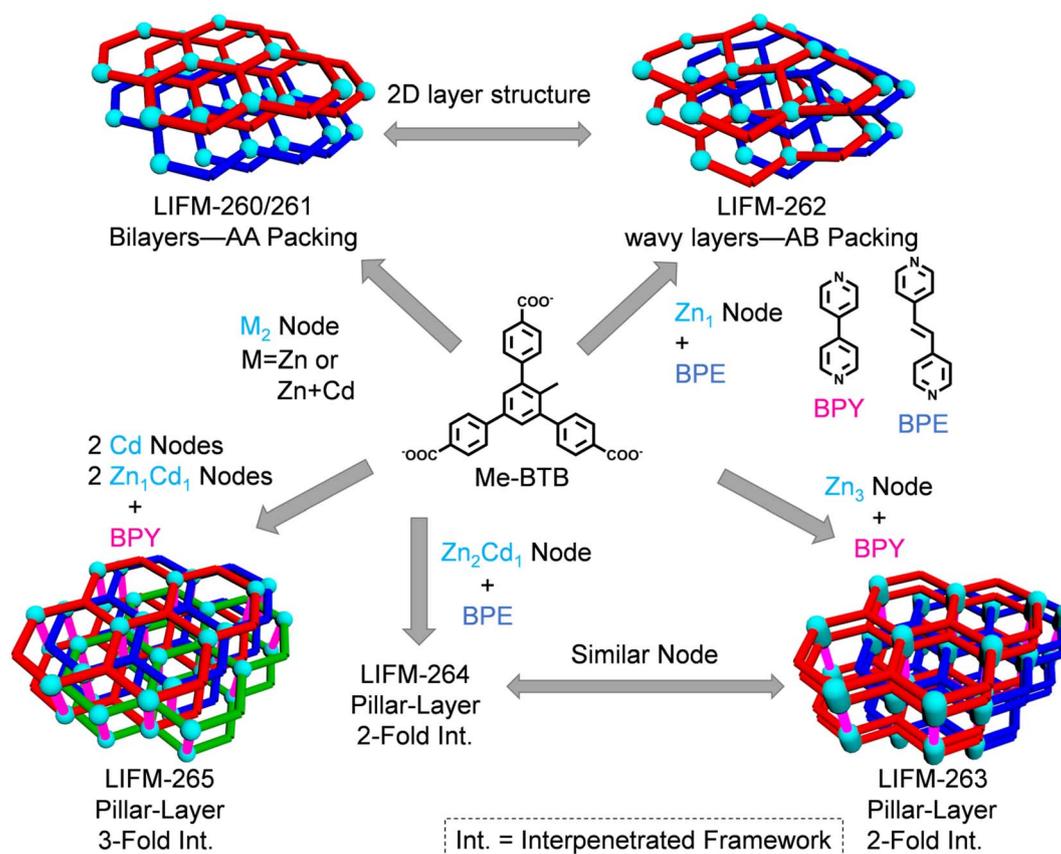

Fig. 1 Structures of a family of Zn/Cd-MOFs (LIFM-260–265) with layer-based structures.

This journal is © The Royal Society of Chemistry 2026

J. Mater. Chem. A, 2026, **14**, 14128–14140 | **14129**

and C_2H_6/CH_4 selectivity. Breakthrough experimental results demonstrated that LIFM-265 exhibits the best separation performance for producing CH_4 (purity >99.8%, yield 7.92 mmol g^{-1} in one cycle) from the ternary $CH_4/C_2H_6/C_3H_8$ (85 : 10 : 5, v/v/v) mixture. Through grand canonical Monte Carlo (GCMC) simulations, we further identified potential adsorption sites for C_3H_8, C_2H_6, and CH_4 that are situated near the metal nodes, as well as the key roles of C–H⋯O and C–H⋯π interactions between hydrocarbons and ligands. This study offers essential perspectives for the development of pillar-layered porous MOFs aimed at enhancing gas adsorption and separation technologies.

2. Results and discussion

2.1 Synthesis and structure

First, the reaction of $Zn(NO_3)_2 \cdot 6H_2O$ with 1,3,5-tris(4-carboxyphenyl)benzene (H_3BTB-Me) in N,N-diethylformamide (DEF), using 1,4-dicarboxybenzene as a modulator at 85 °C for 3 days, yielded colorless rod-shaped crystals of LIFM-260 (Fig. 2). Elemental mapping images (Fig. S8a) show that Zn is homogeneously distributed throughout LIFM-260. Single-crystal X-ray diffraction (SCXRD) analysis revealed that LIFM-260 crystallizes in the triclinic space group $P\bar{1}$. The structure features a binuclear Zn_2 node with the formula of $Zn_2(COO)_3(NO_3)(DEF)_3$ (Fig. 2b). The Zn1(II) and Zn2(II) cations are bridged by three carboxylates from three distinct BTB-Me ligands employing two syn–syn μ_2-η^1:η^1 and one μ_2-η^2:η^1 modes (Fig. S1 in the SI). These three modes simultaneously correspond to the three connection modes of each BTB-Me ligand.[33,34] Zn1(II) exhibits an octahedral coordination mode and additionally coordinates to three DEF molecules via their carbonyl oxygen atoms, while Zn2(II) adopts a pseudo-trigonal-bipyramidal coordination mode, and it additionally coordinates with one nitrate as a terminal ligand (Fig. S2). These 3-connected Zn_1 nodes and 3-connected BTB-Me ligands assemble into a 2D honeycomb-like hexagonal network with a typical **hcb** topology and regular hexagonal pores (Fig. 2c). Subsequently, each pair of 2D networks packs in an ABAB mode along the a-axis and intercalates their coordinated DEF molecules into each other's hexagonal pores, forming an intertwined bilayer 2D grid (Fig. 2d). This bilayer grid then packs closely in an AA stacking manner (Fig. 2e and f), resulting in a nonporous framework, as confirmed by PLATON calculation using a 1.8 Å radius probe.[35]

By reacting $Zn(NO_3)_2 \cdot 6H_2O$, $Cd(NO_3)_2 \cdot 4H_2O$ and H_3BTB-Me in a mixture of DEF and ethanol at 85 °C for 4 days, a colorless rod-shaped crystal LIFM-261 was prepared. Elemental mapping images (Fig. S8b) show that Zn and Cd are homogeneously distributed throughout LIFM-261. SCXRD analysis reveals that LIFM-261 is isostructural with LIFM-260, as evidenced by their very similar unit cell dimensions, identical triclinic $P\bar{1}$ space group, the same **hcb** topology, and nonporous nature (Fig. 2). Notably, LIFM-261 features a heterometallic node [ZnCd(COO)$_3$(NO$_3$)(DEF)$_3$], which is isostructural with the homometallic node [Zn$_2$(COO)$_3$(NO$_3$)(DEF)$_3$] in LIFM-260, wherein a Cd(II) cation replaces the Zn(II) site that coordinates to DEF molecules (Fig. 2b and S3). This successful substitution demonstrates the feasibility of constructing isostructural MOFs
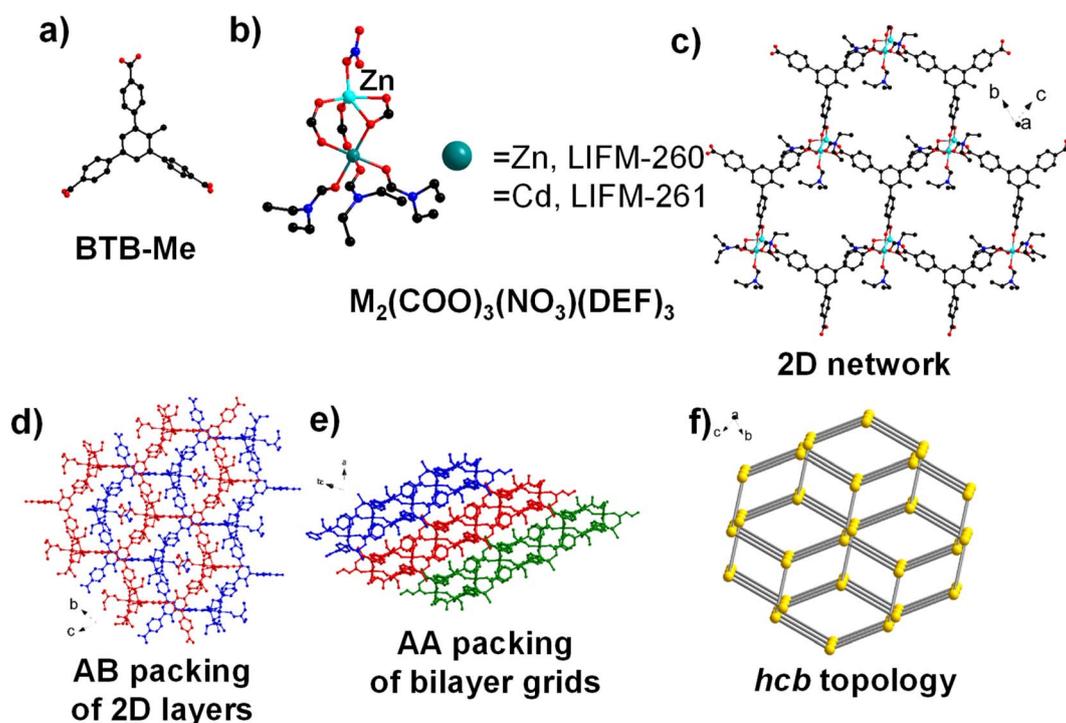

Fig. 2 Structure of LIFM-260/261. (a) Methyl-modified BTB-Me ligand, (b) M$_2$ node, and (c) 2D network. (d) Bilayer grid formed by ABAB packing of the 2D networks. (e) Side view of the AA packing mode of the bilayer grids. (f) **hcb** topology. Color code: black, C; blue, N; red, O; aqua, Zn; teal, Zn or Cd; gold, 3-c node. All hydrogen atoms and disordered methyl groups are omitted for clarity.

14130 | J. Mater. Chem. A, 2026, **14**, 14128–14140

This journal is © The Royal Society of Chemistry 2026

via heterometallic exchange, preserving the overall network topology (Fig. 2c–f).

If the coordinated nitrate incorporated in $(M_2(COO)_3(NO_3)(DEF)_3$, $M_2 = Zn_2$ or Zn/Cd) nodes can be displaced by additional pillar ligands, such a layer structure of LIFM-260/261 can further extend into a 3D framework. At 85 °C, $Zn(NO_3)_2 \cdot 6H_2O$, H_3BTB-Me and auxiliary ligands, namely *trans*-1,2-bis(4-pyridyl)ethane (BPE) (Fig. 3a) and 4,4′-bipyridine (BPY) (Fig. 4a), were reacted in a mixture of *N,N*-dimethylacetamide (DMAC) and water for 4 days, yielding rod-shaped crystals of LIFM-262 and LIFM-263. Elemental mapping images (Fig. S8c) show that Zn is homogeneously distributed throughout LIFM-262. SCXRD analysis indicates that LIFM-262 belongs to the monoclinic space group $P2_1/n$. It features a mononuclear Zn node, [Zn(COO)₃(Py)] (where Py denotes a pyridine ring from BPE), in which each Zn(II) ion adopts a tetrahedral geometry,

coordinated by three carboxylate oxygen atoms from different BTB-Me ligands and one nitrogen atom from a BPE ligand (Fig. 3b and S4). This coordination environment is analogous to that of the Zn site in the heterometallic node of LIFM-261, effectively formed by displacing the coordinated NO_3^- with the BPE pillar. Just as in LIFM-260/261, these 3-connected Zn nodes further link with 3-connected H_3BTB-Me ligands to form a wavy 2D honeycomb-like hexagonal network extended along the *bc* plane (Fig. 3c and d). Since BPE is much longer than DEF, each 2D network can intercalate its BPEs along the *a*-axis into the hexagonal pores of upper two layers and lower two layers (Fig. 3d). These intercalated networks pack in an ABAB manner (viewed along the *a*-axis) to construct the MOF, which shares the same 2D network packing mode as LIFM-260/261 and features one type of 6.4 Å 1D channels along the *a*-axis; the total pore
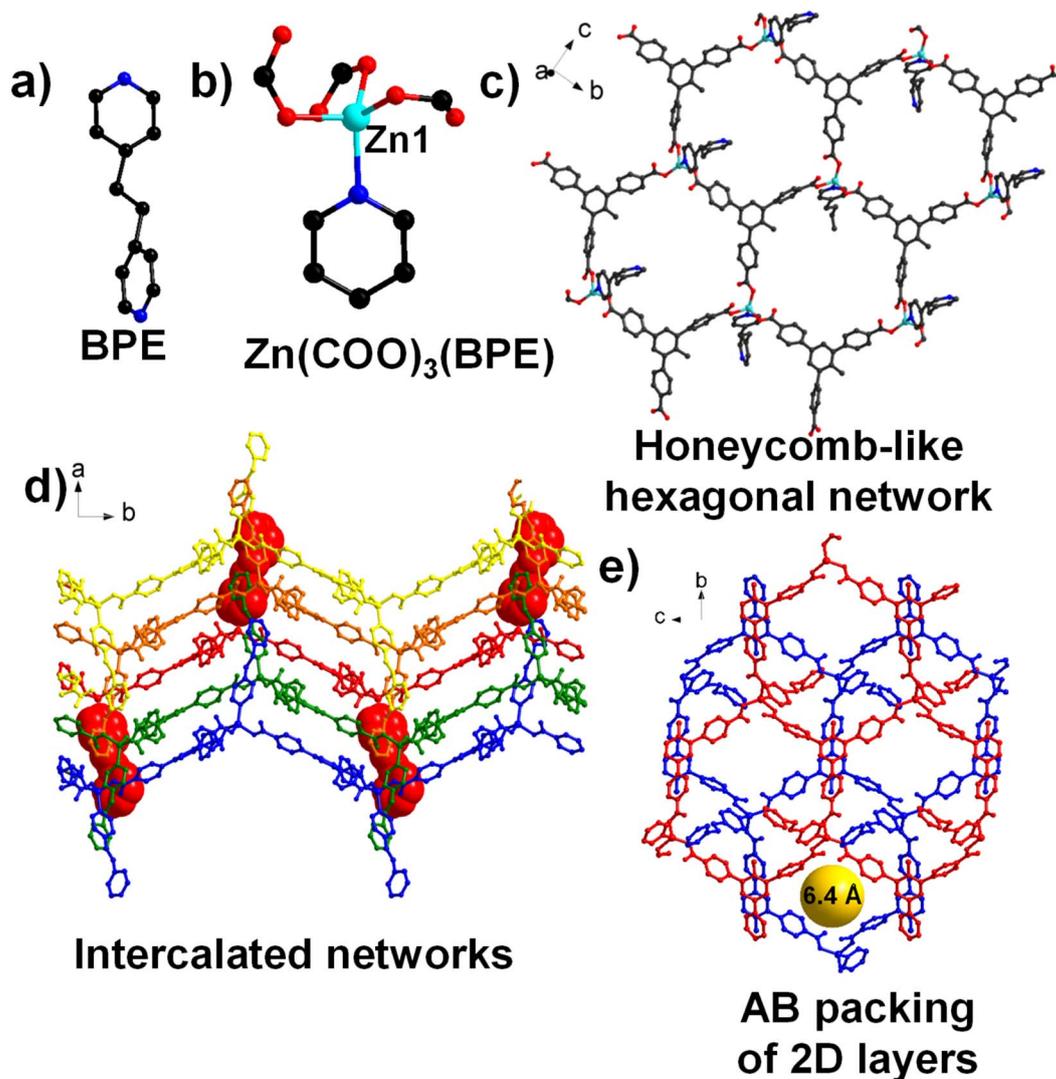

Fig. 3 Structure of LIFM-262. (a) Ligand BPE, (b) Zn node, and (c) honeycomb-like hexagonal network. (d) Intercalated networks of LIFM-262: each layer is labeled with a different color, and BPE ligands of the red layer are shown in space-filling mode. (e) ABAB packing mode of the 2D layers. Color code: black, C; blue, N; red, O; aqua, Zn. All hydrogen atoms, disordered methyl groups and disordered BPE ligands are omitted for clarity.
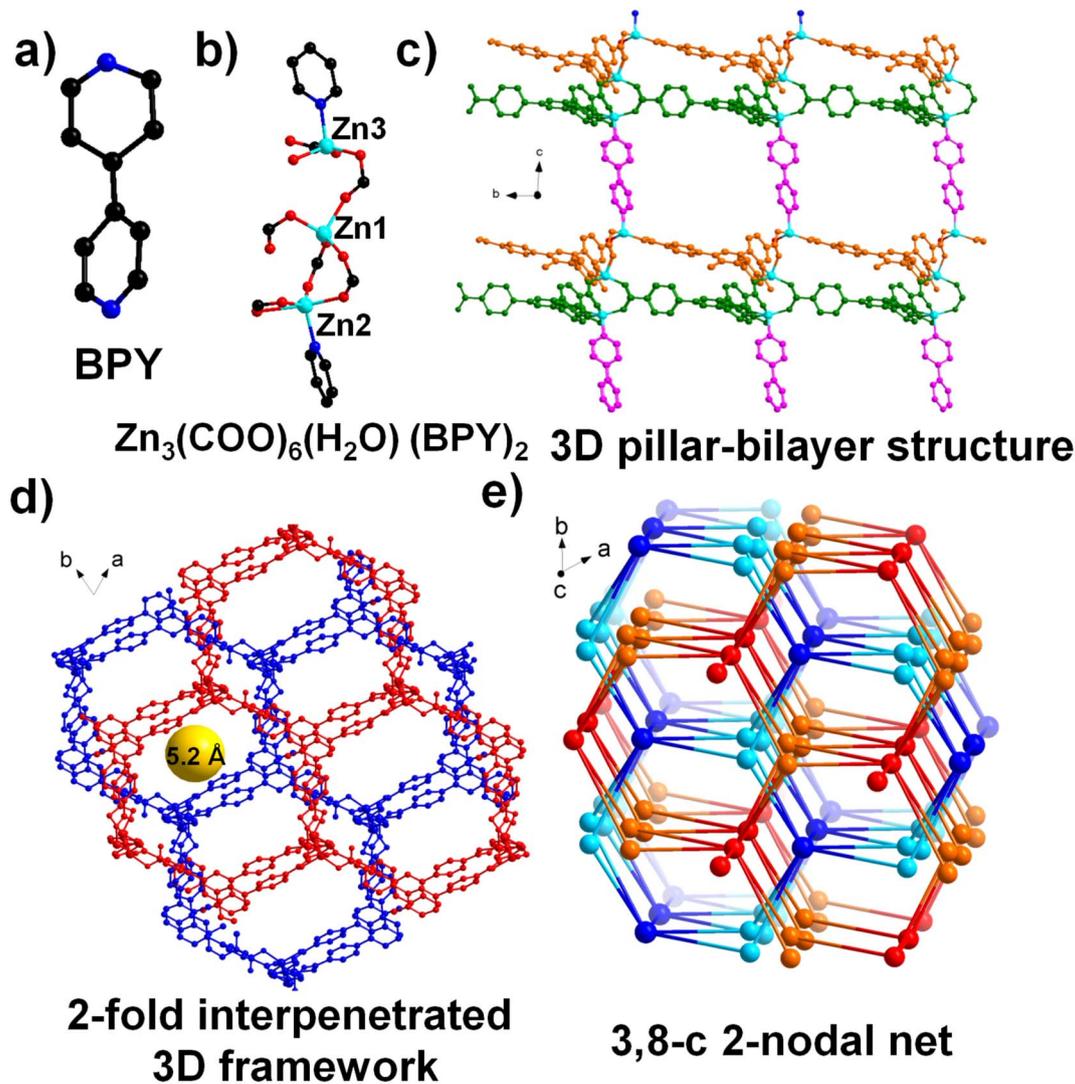
Fig. 4 Structure of LIFM-263. (a) Ligand BPY and (b) Zn_3 node. (c) 3D pillar-bilayer structure: green, lower layer; orange, upper layer; pink, BPY pillars. (d) 2-Fold interpenetrated 3D framework: blue/red, subnetworks; gold pillars, 1D channels. (e) The topology: red/blue, 8-c nodes; orange/light blue, 3-c nodes. Color code: black, C; blue, N; red, O; aqua, Zn. All hydrogen atoms and disordered methyl groups are omitted for clarity.

volume is 0.15 cm^3 g^{-1} (calculated by PLATON with a 1.8 Å radius probe; Fig. 2f).

Elemental mapping images (Fig. S8d) show that Zn is homogeneously distributed throughout LIFM-263. SCXRD analysis reveals that LIFM-263 crystallizes in the triclinic $P\bar{1}$ space group. It features a pseudo-hourglass Zn_3 node ($Zn_3(COO)_6(H_2O)(Py)_2$) linked to six BTB-Me and two BPY ligands, with two types of BTB-Me ligands (BTB-Me-1/2) each connecting three Zn_3 nodes: namely, BTB-Me-1 links Zn1/Zn2, and BTB-Me-2 links Zn1/Zn3 (Fig. S5). The lower Zn2(II) is bridged to the middle Zn1(II) by two BTB-Me-1 in syn–syn μ_2-η^1:η^1 mode and coordinates to one BTB-Me-1 in bidentate chelating mode, consistent with the three connection modes of BTB-Me-1 (Fig. 4b and S1). On the other hand, the upper Zn3(II) is bridged to Zn1(II) by one BTB-Me-2 in syn–anti μ_2-η^1:η^1 mode, and each of these two Zn(II)s additionally coordinates to one more BTB-Me-2 in monodentate mode, corresponding to the three connection modes of the BTB-Me-2 ligand. Thus, Zn1 adopts a tetrahedral geometry. Besides BTB-Me ligands, Zn2 coordinates to one BPY (exhibiting a pseudo-square-pyramidal geometry) while Zn3 coordinates to one BPY and one water molecule (adopting a tetrahedral geometry). Zn_3 nodes connect to three BTB-Me-1 ligands to form a lower layer and to three BTB-Me-2 ligands to form an upper layer, resulting in a 2D honeycomb-like hexagonal bilayer extended along the ab plane with the typical **hcb** topology, which is similar but not identical to the bilayer of LIFM-260/261 (Fig. 4c and d). These bilayers pack in AA mode (viewed along the c-axis) are further connected into a 3D subnetwork through BPY ligands along the c-axis, and two subnets interpenetrate to construct a 3D 2-fold interpenetrated pillar-layer structure with 5.2 Å 1D channels along the c-axis, representing the first successful example of our pillar-layer MOF design (Fig. 4d). Correspondingly, its theoretical total pore volume is calculated to be 0.38 cm^3 g^{-1} by PLATON using

14132 | J. Mater. Chem. A, 2026, 14, 14128–14140

This journal is © The Royal Society of Chemistry 2026

a 1.8 Å radius probe. From the topological viewpoint, the Zn_3 nodes are 8-connected nodes, while the BTB-Me ligands are 3-connected nodes. One subnetwork can be simplified as a 3,8-*c* 2-nodal net with stoichiometry $(3-c)_2(8-c)$ and the topological point symbol $\{4^3 \cdot 6^{24} \cdot 8\}\{4^3\}_2$, which is previously unreported (Fig. 4e).

The successful formation of Zn/Cd heterometallic nodes in LIFM-261 encouraged us to introduce Cd(ɪɪ) into the LIFM-262 reaction system, yielding a colorless crystal named LIFM-264. Elemental mapping images (Fig. S8e) show that Zn and Cd are homogeneously distributed throughout LIFM-264. Notably, LIFM-264 is structurally more similar to LIFM-263 than to LIFM-262: both crystallize in the triclinic $P\bar{1}$ space group and feature a pseudo-hourglass M_3 node ($Zn_2Cd(COO)_6(H_2O)(Py)_2$ for LIFM-264) linked to six BTB-Me and two BPE ligands (Fig. 5a). This heterometallic node incorporates two BTB-Me ligand types (BTB-Me-1/2), each connecting three Zn_2Cd nodes—specifically, BTB-Me-1 links Cd1/Zn1, and BTB-Me-2 links Cd1/Zn2 (Fig. S6). The Zn_2Cd node exhibits distinct coordination modes from those in LIFM-263. The lower Zn1(ɪɪ) is bridged to the middle Cd1(ɪɪ) *via* two BTB-Me-1 carboxylates (*syn–syn* μ_2-η^1:η^1 and μ_2-η^2:η^1 modes), and coordinates to one BTB-Me-1 carboxylate in bidentate chelating mode and one BPE ligand, forming a pseudo-octahedral geometry (Fig. S1). The upper Zn2(ɪɪ) connects to Cd1(ɪɪ) through three BTB-Me-2 carboxylates (*syn–syn* μ_2-η^1:η^1 mode) and further coordinates to another BPE ligand, adopting a tetrahedral geometry. Cd1(ɪɪ) additionally binds one water molecule, resulting in an octahedral coordination environment (Fig. 5a). Ignoring M_3 node details, LIFM-264 shares the same network composition and topology as LIFM-263. Overall, each BTB-Me ligand acts as a 3-connected node connecting three Zn_2Cd heterometallic nodes. Each Zn_2Cd node functions as an 8-connected node, connecting

three BTB-Me-1 ligands (lower layer) and three BTB-Me-2 ligands (upper layer) to form a 2D bilayer (along the *ab* plane; Fig. 5b), and is further linked by two BPE pillars (along the *c*-axis) to yield a 3D subnetwork. These subnetworks interpenetrate to form a 2-fold interpenetrated framework with 5.6 Å 1D channels along the *c*-axis and a theoretical total pore volume of 0.42 cm^3 g^{-1} (PLATON calculation, 1.8 Å probe; Fig. 5c). Consistent with LIFM-263, it exhibits the unreported 3, 8-*c* 2-nodal topology (Fig. 4d).

As pure Zn nodes and BPY ligands did not produce a 3D pillar-layer framework in LIFM-263, while Zn/Cd heterometallic nodes and BPE ligands constructed a porous 3D pillar-layer framework in LIFM-264, the reaction conditions of LIFM-264 were used, except that BPE was replaced with BPY. As expected, a new Zn/Cd MOF named LIFM-265 was produced. Elemental mapping images (Fig. S8f) show that Zn and Cd are homogeneously distributed throughout LIFM-265. SCXRD analysis indicates that LIFM-265 belongs to the triclinic space group $P2_1/n$. Fig. 6a illustrates the geometries of the two types of mononuclear metal nodes (Cd1 and Cd4) and two types of binuclear heterometallic nodes (Zn1–Cd2 and Zn2–Cd3). Additionally, there are four types of BTB-Me and three types of BPY ligands, designated as BTB-Me-1/2/3/4 and BPY-1/2/3, respectively (Fig. S7). The seven-coordinate Cd1(ɪɪ) exhibits a distorted pentagonal-bipyramidal geometry: three carboxylates (two from BTB-Me-1 and one from BTB-Me-3), all in a bidentate chelating mode, form a fan-like equatorial plane, while a nitrogen atom from a BPY-1 ligand occupies the axial position (along the rotation axis of the fan). The six-coordinate Cd4(ɪɪ) possesses a similarly distorted square-bipyramidal geometry: three carboxylates form a pseudo-fan (two from BTB-Me-2/3 in bidentate chelating mode; one from BTB-Me-4 in monodentate mode), and the N atom of one BPY-2 occupies the axial position. For the Zn1–Cd2 heterometallic
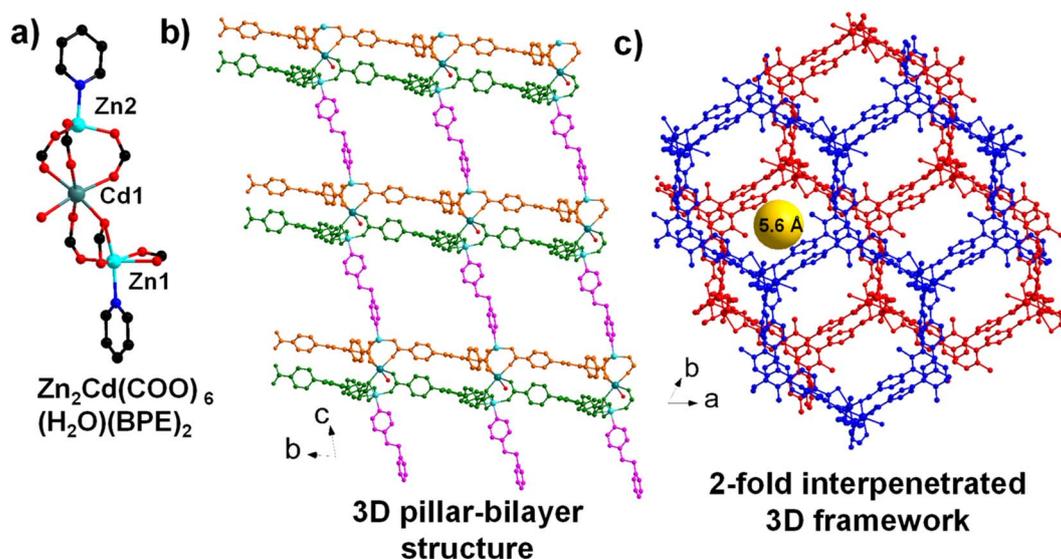

Fig. 5 Structure of LIFM-264. (a) Zn_2Cd node. (b) 3D pillar–bilayer structure: green, lower layer; orange, upper layer; pink, BPE pillars. (c) 2-Fold interpenetrated 3D framework: blue/red, subnetworks; gold pillars, 1D channels. Color code: black, C; red, O; aqua, Zn; teal, Cd. All hydrogen atoms and disordered methyl groups are omitted for clarity.
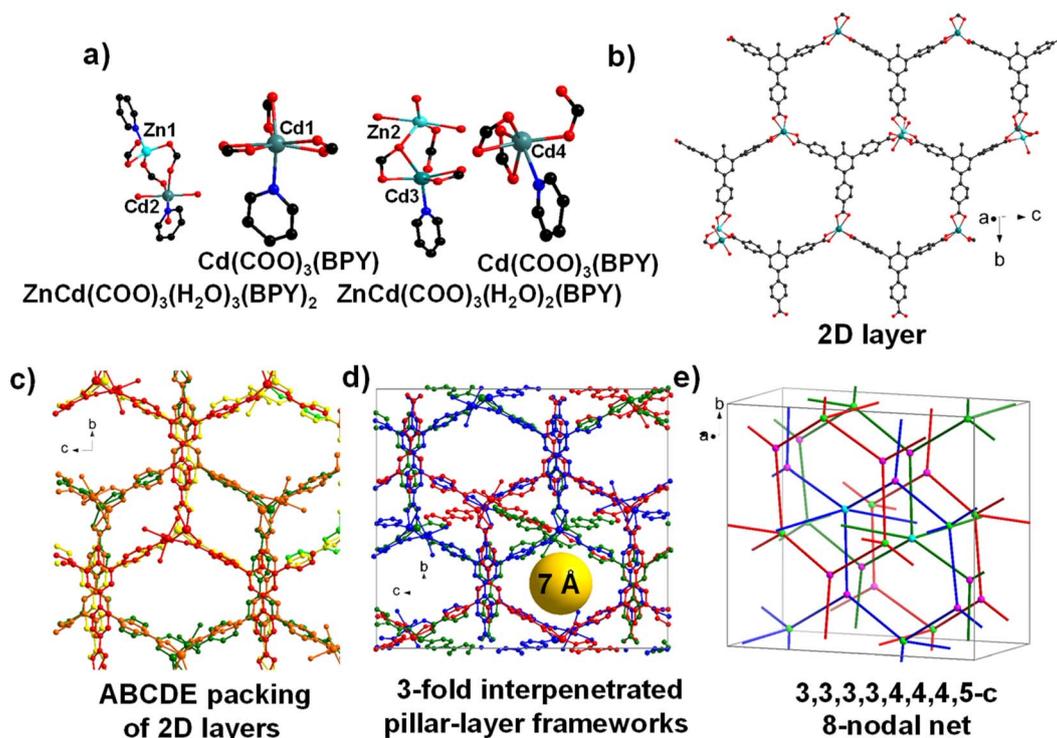
Fig. 6 Structure of LIFM-265. (a) Two types of mononuclear Cd nodes and two types of Zn/Cd heterometallic nodes. (b) 2D layer. (c) ABCDE packing mode of the 2D layers in the same network: red, layer A; orange, layer B; yellow, layer C; green, layer D; bright green, layer E. (d) 3-Fold interpenetration of 3D frameworks. (e) Topology of LIFM-265. Color code: black, C; red, O; aqua, Zn; teal, Cd. All hydrogen atoms are omitted for clarity.

node, the two cations are bridged by two carboxylates (one from BTB-Me-1 and one from BTB-Me-2) *via* the *syn–syn* μ_2-η^1:η^1 mode (Fig. S1). Zn1(II) is further coordinated to one carboxylate of BTB-Me-3 in bidentate chelating mode and one BPY-2 ligand, forming a distorted square-pyramidal coordination geometry. Cd2(II) is coordinated to three additional water molecules and one BPY-2 ligand, exhibiting an octahedral coordination geometry. The Zn2–Cd3 heterometallic node has a distinct structure: the two cations are bridged by two carboxylates (one from BTB-Me-2 in *syn–syn* μ_2-η^1:η^1 mode and one from BTB-Me-4 in μ_2-η^2:η^1 mode). Zn2(II) further coordinates to three water molecules—similar to Cd1(II)—forming a distorted square-pyramidal coordination geometry. In contrast, Cd3(II) coordinates to one BTB-Me-4 carboxylate in bidentate chelating mode and one BPY-3 ligand, forming a distorted square-bipyramidal coordination geometry. Overall, each BTB-Me ligand acts as a 3-connected node linking three metal nodes. Each metal node connects three BTB-Me ligands to form a 2D plane, which packs in an ABC-DEABCDE mode, and is further linked into a 3D subnetwork by one BPY ligand (for Cd1, Cd4, and Zn2–Cd3 nodes) or two BPY ligands (for Zn1–Cd2 nodes), resulting in 4-connected or 5-connected nodes, respectively (Fig. 6). Finally, the 3D subnetworks interpenetrate in a 3-fold manner. Hence, LIFM-265 can be simplified to an unreported 3,3,3,3,4,4,4,5-c 8-nodal net with the stoichiometry (3-*c*)(3-*c*)(3-*c*)(3-*c*)(4-*c*)(4-*c*)(4-*c*)(5-*c*) and a topological point symbol of $\{6^3\}_4\{6^5 \cdot 8\}\{6^6\}_2\{6^9 \cdot 10\}$ (Fig. 6). The 2D plane extends approximately along the *bc* plane with a slight tilt (*ca.*

15°) relative to it (Fig. 6). There is one type of 7 Å 1D channel along the *a*-axis, and the theoretical total pore volume is 0.25 cm³ g⁻¹ (PLATON calculation with a 1.8 Å probe; Fig. 6).

2.2 Phase purity and porosity

The phase purity of the six MOFs (LIFM-260–265) was verified by powder X-ray diffraction (PXRD) (Fig. S9–S14), showing that the experimental patterns match well with the simulated ones and confirming the high purity of the MOF samples. The thermal stability of the six MOFs was evaluated using thermogravimetric analysis (TGA) and variable-temperature PXRD (VT-PXRD). The results show that LIFM-260–265 remain stable at 225 °C, 125 °C, 350 °C, 375 °C, 300 °C, and 300 °C, respectively (Fig. S18–S24). In addition, the chemical stability of the three porous MOFs (*vide infra*) was evaluated by exposing the samples to hot water (80 °C) and aqueous solutions with various pH values (0.1 M HCl, 0.1 M NaOH, and 1 M NaOH). This showed that all three MOFs retained their structural integrity, indicating exceptional robustness (Fig. S15–S17).

N₂ (77 K) adsorption measurements were conducted to assess the porosity of the six MOFs. As predicted by the total pore volume calculation of PLATON, LIFM-260–262 showed no porosity (Fig. 7a). Therefore, no further research will be conducted on them. In contrast, LIFM-263–265 exhibit type I microporous adsorption isotherms. The Brunauer–Emmett–Teller (BET) surface areas (S_{BET}) and total pore volumes follow the order of LIFM-264 (1030 m² g⁻¹ and 0.43 cm³ g⁻¹) > LIFM-
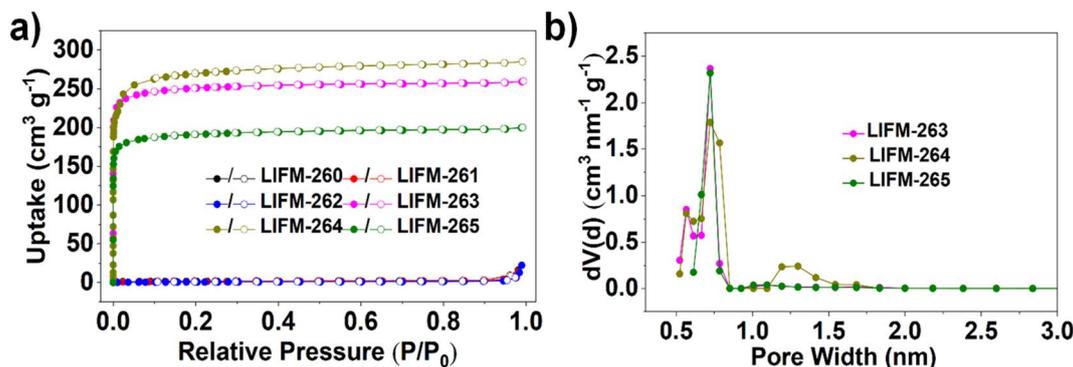
Fig. 7 (a) N_2 adsorption isotherms of LIFM-260–265 at 77 K. Solid symbols: adsorption; open symbols: desorption. (b) Pore size distribution of LIFM-263–265 calculated from the QSDFT model.

265 (763 m^2 g^{-1} and 0.31 cm^3 g^{-1}) > LIFM-263 (718 m^2 g^{-1} and 0.30 cm^3 g^{-1}) (Table S4). This trend also matches the theoretical total pore volume calculated *via* PLATON, further demonstrating effective pore-nanospace modulation by introducing pillar ligands of different lengths. Pore sizes were determined from the peak positions in the pore size distributions (PSDs), calculated *via* the Quenched Solid Density Functional Theory (QSDFT) method based on the adsorption branch. The corresponding pore sizes are 0.57 and 0.72 nm for LIFM-263, 0.57, 0.72 nm, and 1.25 nm for LIFM-264, and 0.72 nm for LIFM-265 (Fig. 7b).

2.3 C_1–C_3 light hydrocarbon adsorption

To evaluate the gas separation performance, CH_4, C_2H_6, and C_3H_8 adsorption isotherms were measured at 273 K, 283 K, and 298 K, respectively (Fig. 8a–c). At 298 K and 1 bar, the C_2H_6 and

C_3H_8 uptakes of the MOFs follow the same order: LIFM-264 (79.0 cm^3 g^{-1}) > LIFM-263 (69.6 cm^3 g^{-1}) > LIFM-265 (48.5 cm^3 g^{-1}) for C_2H_6, and LIFM-264 (100.0 cm^3 g^{-1}) > LIFM-263 (76.3 cm^3 g^{-1}) > LIFM-265 (53.3 cm^3 g^{-1}) for C_3H_8. All MOFs exhibit significantly higher C_2H_6 and C_3H_8 uptake capacities compared to CH_4, suggesting a preferential adsorption for C_2H_6 and C_3H_8. This can be attributed to the greater polarizability and larger kinetic size of C_2H_6 and C_3H_8 molecules, leading to stronger interactions between the gases and the frameworks in the confined pore nanospace.[36] Thereafter, adsorption–desorption cycling of CH_4, C_2H_6, and C_3H_8 on LIFM-263, LIFM-264, and LIFM-265 was tested at 298 K, demonstrating that the internal surface remained intact even after repeated exposure to hydrocarbon gas molecules (Fig. S28–S30). It is worth noting that the introduction of pillar ligands not only endows LIFM-263–265 with a pore environment containing more aromatic rings, thereby enhancing the C–H···π interactions between the
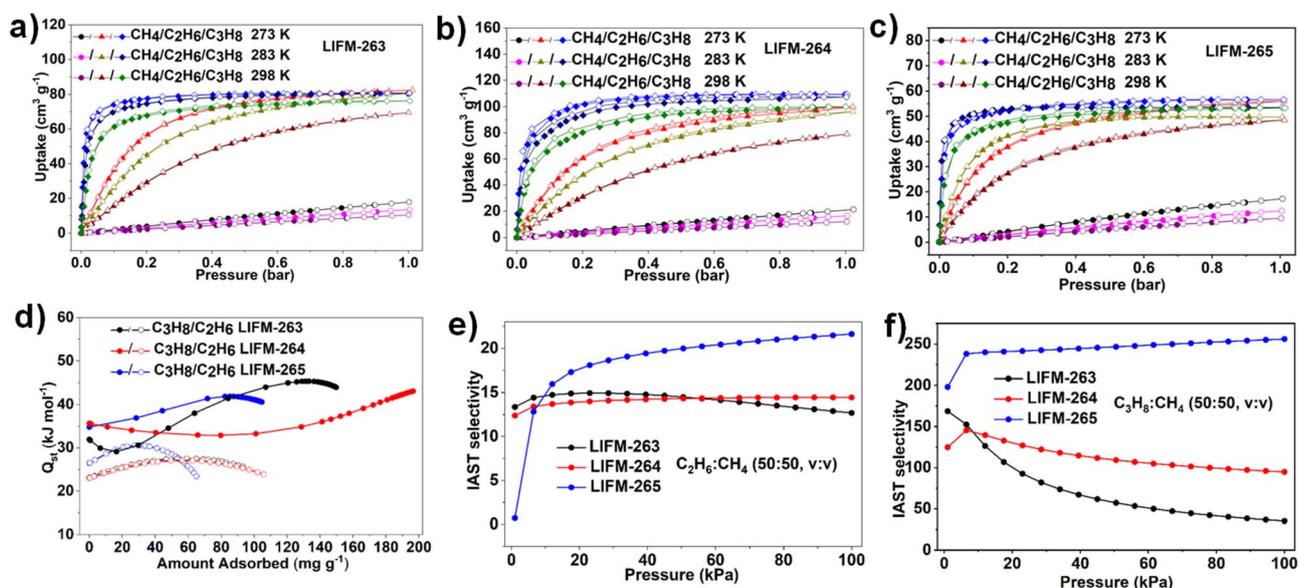

Fig. 8 Gas adsorption and separation performance of LIFM-263, LIFM-264, and LIFM-265. (a–c) CH_4, C_2H_6 and C_3H_8 adsorption isotherms of the MOFs at 273 K, 283 K and 298 K, respectively. (d) Q_{st} curves of C_2H_6 and C_3H_8 adsorption of the MOFs as a function of surface coverage. (e) IAST selectivities of the MOFs for C_2H_6/CH_4 (50 : 50, v/v) at 298 K. (f) IAST selectivities of the MOFs for C_3H_8/CH_4 (50 : 50, v/v) at 298 K.

hydrocarbon molecules and frameworks, but also finely regulates the pore size and pore volume, which may affect the kinetic separation of C_2–C_3 light hydrocarbons from CH_4. These results suggest that the aromatic-functionalized pillar-layer MOFs may exhibit good potential for separating low-concentration C_2–C_3 light hydrocarbons from CH_4.

The isosteric heats of adsorption (Q_{st}) for C_2H_6 and C_3H_8 were determined using the Clausius–Clapeyron equation based on the gas adsorption isotherms at 273 K, 283 K, and 298 K.[37] As shown in Fig. 8d, the Q_{st} values (at zero coverage) of C_3H_8 and C_2H_6 for LIFM-263–265 follow the sequence C_3H_8 > C_2H_6, indicating that the interactions between C_3H_8 and the MOFs were stronger than those between C_2H_6 and the frameworks. For LIFM-263, the experimental Q_{st} value of C_3H_8 at near zero loading is 31.9 kJ mol^{-1}, which is lower than those of LIFM-265 (34.8 kJ mol^{-1}) and LIFM-264 (35.7 kJ mol^{-1}). The experimental Q_{st} values of C_2H_6 for LIFM-265 and LIFM-263 were 26.5 kJ mol^{-1} and 23.1 kJ mol^{-1}, while the minimum Q_{st} value of C_2H_6 with LIFM-264 was 23.0 kJ mol^{-1} at near zero loading. Comparison of the BET specific surface area, pore volume, C_2H_6/C_3H_8 adsorption capacities, and Q_{st} values of the three MOFs reveals no obvious linear correlation between these physicochemical parameters and the target gas adsorption behaviors. This may be attributed to the synergistic effects of multiple structural factors (*e.g.*, pore confinement, active site distribution, and molecular interaction types) on the adsorption process.

The ideal adsorption solution theory (IAST) model, combined with dual-site Langmuir–Freundlich (DSLF) fitting, was used to calculate the C_2H_6/CH_4 and C_3H_8/CH_4 selectivities at various mixing ratios (Fig. 8e, f, S37, S38 and Table S5).[38] For the C_2H_6/CH_4 (50 : 50, v/v) mixture, the IAST selectivities at 298 K and 1 bar follow a descending trend of LIFM-265 (22) > LIFM-264 (14) > LIFM-263 (13). In contrast, for the C_2H_6/CH_4 (10 : 90, v/v) mixture under the same temperature and pressure conditions, the IAST selectivities show a different descending order: LIFM-265 (19) > LIFM-263 (15) > LIFM-264 (14). For C_3H_8/CH_4 mixtures (both 5 : 95 and 50 : 50, v/v), the IAST selectivities exhibit a consistent descending trend of LIFM-265 (240/256) > LIFM-264 (140/95) > LIFM-263 (129/35), which is the same order of C_2H_6/CH_4 (50 : 50) selectivities. Notably, the selectivities of LIFM-265 (with medium BET surface area and pore size) for C_2H_6/CH_4 and C_3H_8/CH_4 mixtures under ambient conditions (298 K, 1 bar) are all superior to those of LIFM-263/264, and also to the C_2/C_1 and C_3/C_1 selectivities (298 K, 50 : 50) of several previously reported MOF materials, such as ANPC-2-700 (14/163),[39] FJI-H22 (12/145),[40] JLU-Liu5 (18/108),[41] JUC-100 (11/80),[42] and MIL-101-Fe (15/25)[43] (Table S5), further highlighting its potential for methane purification.

2.4 Breakthrough experiment

To assess the practical separation efficiency, transient breakthrough tests were performed on LIFM-263–265 under ambient conditions using a $CH_4/C_2H_6/C_3H_8$ (85 : 10 : 5, v/v/v) ternary mixture passed through a fixed-bed column at a flow rate of 5 mL min^{-1} (Fig. 9 & Table S6).

For all three MOFs, CH_4 was first eluted, while C_2H_6 and C_3H_8 were retained in the fixed-bed column for a certain period before being sequentially eluted. The retention time of C_2H_6 is similar for LIFM-263 (20 min g^{-1}) and LIFM-265 (22 min g^{-1}), while that for LIFM-264 (15 min g^{-1}) is shorter. In contrast, the retention time of C_3H_8 shows a decreasing trend of LIFM-263 (150 min g^{-1}) > LIFM-265 (140 min g^{-1}) > LIFM-264 (112 min g^{-1}). Notably, the C_2H_6 capture capacity is highest for LIFM-265 (0.56 mmol g^{-1}), followed by LIFM-263 (0.41 mmol g^{-1}) and
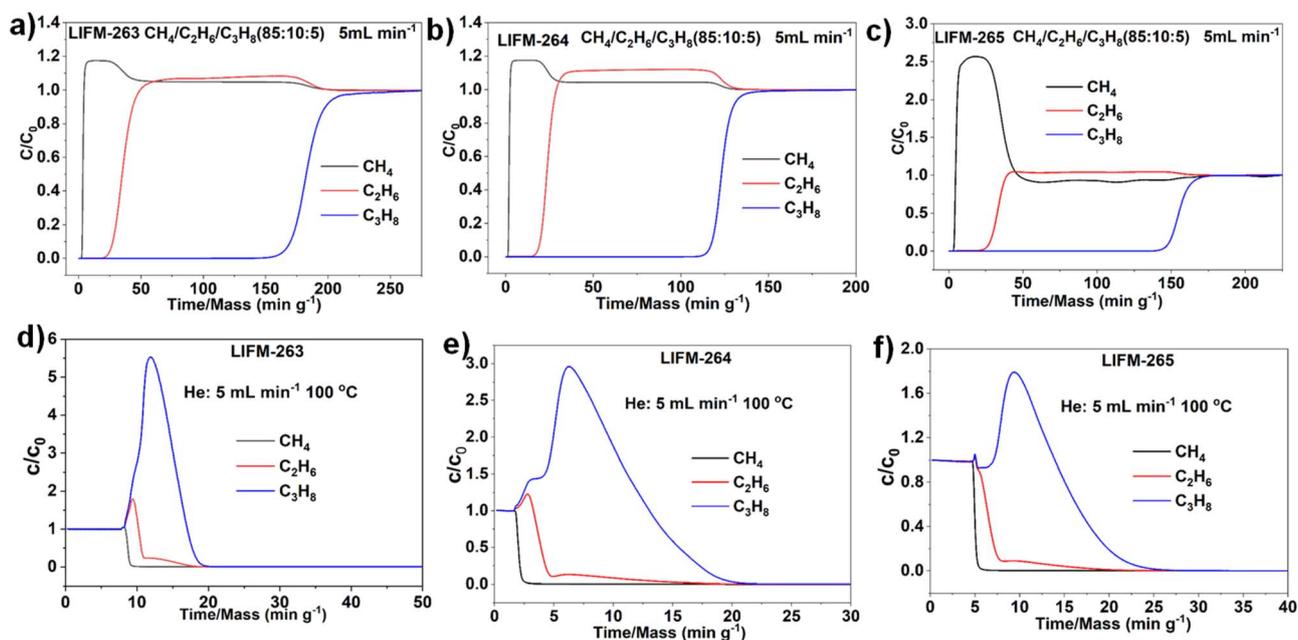

Fig. 9 Transient breakthrough curves (a–c) of a $CH_4/C_2H_6/C_3H_8$ (85 : 10 : 5, v/v/v) mixture for LIFM-263–265 and (d–f) their desorption curves.

14136 | *J. Mater. Chem. A*, 2026, **14**, 14128–14140

This journal is © The Royal Society of Chemistry 2026

LIFM-264 (0.07 mmol g^{-1}), in contrast to the C$_3$H$_8$ capture capacity, which is greatest for LIFM-263 (2.39 mmol g^{-1}) > LIFM-265 (1.85 mmol g^{-1}) > LIFM-264 (1.41 mmol g^{-1}). Although the CH$_4$ elution times are relatively similar, the high-purity CH$_4$ yield of LIFM-265 (purity: >99.8%) is 7.92 mmol g^{-1}, which is generally twice those of LIFM-263 (4.45 mmol g^{-1}, purity: >99.7%) and LIFM-264 (3.37 mmol g^{-1}, purity: >99.6%). This high yield is attributed to the strong concentration over-shoot of CH$_4$ ($C/C_0 > 1$), where C$_2$H$_6$/C$_3$H$_8$ preferentially displace adsorbed CH$_4$, increasing the recovery of high-purity CH$_4$. Despite having the smallest surface area, pore volume, and single-component gas adsorption capacities, LIFM-265 exhibits the most outstanding separation performance, which is consistent with its IAST-predicted selectivity. This indicates that the pore confinement effect plays a significant role in the dynamic separation of the CH$_4$/C$_2$H$_6$/C$_3$H$_8$ ($85:10:5$, v/v/v) ternary mixture—strengthening the competitive adsorption of C$_2$H$_6$/C$_3$H$_8$ and promoting the concentration overshoot of CH$_4$. In contrast, LIFM-264 (with the largest pore diameter) exhibits the shortest C$_2$/C$_3$ retention times, the lowest high-purity CH$_4$ yield (3.37 mmol g^{-1}), and the lowest C$_3$H$_8$ capture capacity (1.41 mmol g^{-1}). This may be attributed to its large pore diameter, which results in rapid breakthrough behavior.

Multiple cyclic breakthrough tests were performed on the three MOFs, showing nearly identical gas retention times to those of the initial breakthrough curves, indicating excellent durability and recyclability (Fig. S39–S41).

2.5 Theoretical calculations

We further explored the gas adsorption mechanism through theoretical calculations using the grand canonical Monte Carlo (GCMC) method.[44,45]

The density distribution results for CH$_4$/C$_2$H$_6$/C$_3$H$_8$ at 1 bar and 298 K in the three MOFs reveal that all gas molecules are predominantly situated in the 1D channels (Fig. S42 and S43), and for the same MOF, the gas density within the channels increases progressively with increasing gas molecular size—suggesting a gradual strengthening of the gas-framework interactions. Additionally, interconnections between the 1D channels are also observed for LIFM-263–264. The calculated C$_3$H$_8$ binding energies follow the order: LIFM-264 (39.1 kJ mol^{-1}) > LIFM-265 (38.1 kJ mol^{-1}) > LIFM-263 (36.2 kJ mol^{-1}), which is consistent with the experimental Q_{st} results. Additionally, the calculated C$_2$H$_6$ binding energies are highest for LIFM-265 (27.8 kJ mol^{-1}), followed by LIFM-263 (26.6 kJ mol^{-1}) and LIFM-264 (25.7 kJ mol^{-1}), and this is also
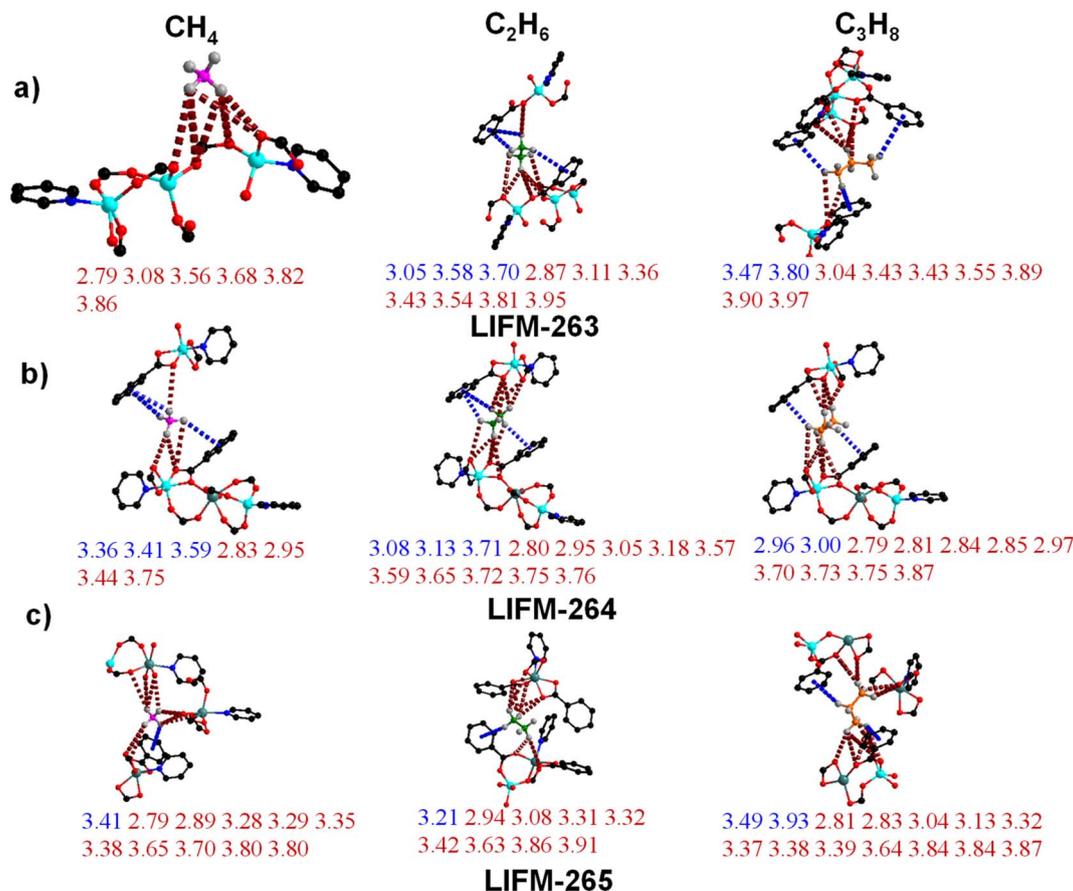

Fig. 10 GCMC simulated primary absorption sites of CH$_4$/C$_2$H$_6$/C$_3$H$_8$ in (a) LIFM-263, (b) LIFM-264, and (c) LIFM-265. Color code: black, C; blue, N; red, O; aqua, Zn; teal, Cd; pink-gray, CH$_4$; green-gray, C$_2$H$_6$; orange-gray, C$_3$H$_8$. The hydrogen atoms of the MOFs have been omitted for clarity. Interaction type: blue, C–H⋯π; dark red, C–H⋯O.

This journal is © The Royal Society of Chemistry 2026

J. Mater. Chem. A, 2026, **14**, 14128–14140 | **14137**

consistent with the Q_{st} results (Table S7). Meanwhile, the binding energies of C_2H_6 and C_3H_8 are significantly higher than those of CH_4 (15.2–18.0 kJ mol^{-1}) for all three MOFs, which is consistent with the experimental findings that they can effectively separate C_2–C_3 light hydrocarbons from CH_4 (Fig. 9). GCMC simulation results demonstrate that a CH_4 molecule located at the primary adsorption site of LIFM-263 near the hourglass Zn_3 node is bound to the O atoms of the carboxylate ligands via six C–H···O interactions (ranging from 2.79 to 3.86 Å; Fig. 10a). For C_2H_6, seven C–H···O interactions (2.87–3.95 Å) and three C–H···π interactions (3.05–3.70 Å)—derived from two Zn_3 nodes—are observed, indicating more extensive interactions with the framework. C_3H_8 exhibits a similar binding mode, involving seven C–H···O interactions (3.04–3.97 Å) and two C–H···π interactions (3.47–3.80 Å). Similarly to LIFM-263, the gas molecules are all primarily adsorbed by the carboxylates and phenyl rings around the Zn centers of two hourglass Zn_2Cd nodes in LIFM-264. A CH_4 molecule is attracted via four C–H···O (2.83–3.75 Å) and three C–H···π (3.36–3.59 Å) interactions; C_2H_6 is bound via ten C–H···O (2.80–3.76 Å) and three C–H···π (3.08–3.71 Å) interactions, while C_3H_8 is bound via nine C–H···O (2.84–3.87 Å) and two C–H···π (2.96–3.00 Å) interactions—exhibiting more interactions with shorter distances and hence stronger attractions compared with those of CH_4. The adsorption sites of LIFM-265 are analogous to those of LIFM-263 and LIFM-264, with interactions categorized into C–H···O and C–H···π types. Specifically, a CH_4 molecule anchors at the primary adsorption site, which is surrounded by Cd1, Cd4, and Zn1–Cd2 nodes, via ten C–H···O (2.79–3.80 Å) and one C–H···π (3.41 Å) interaction; C_2H_6, located between Cd1 and Zn2–Cd3 nodes, forms stable binding through eight C–H···O (2.94–3.91 Å) and one C–H···π (3.21 Å) interaction; C_3H_8, surrounded by Cd1 and two Zn2–Cd3 nodes, achieves stronger adsorption via twelve C–H···O (2.81–3.87 Å) and two C–H···π (3.93–3.94 Å) interactions—characterized by a greater number of interactions relative to CH_4, which translates to enhanced gas-framework attraction. Overall, the adsorption behaviors of CH_4, C_2H_6, and C_3H_8 in LIFM-263–265 exhibit consistent core characteristics: their interaction types are uniformly categorized into C–H···O and C–H···π, with primary adsorption sites localized near the metal nodes (Zn_3 for LIFM-263, Zn_2Cd for LIFM-264, and Cd and ZnCd for LIFM-265) and adjacent carboxylates or phenyl rings. Across the three MOFs, a universal trend emerges wherein C_2H_6 and C_3H_8 form more interactions with the framework compared to CH_4, translating to stronger gas–framework interactions. This consistency in adsorption inter-action patterns—despite subtle differences in the number of interactions and specific bond length ranges among the three materials—highlights the structural rationality of the metal node–carboxylate/phenyl ring motif in regulating light hydrocarbon adsorption, laying a solid foundation for interpreting their gas separation performance.

3. Conclusion

We successfully synthesized six layered Zn- and Zn/Cd-MOFs consisting of tricarboxylate ligand layers and bipyridine pillars, three of which possess a pillar-layer structure and high porosity. Among them, LIFM-265—with optimized nanopores and aromatic ring functionalization—effectively purifies CH_4 by capturing low-concentration C_2H_6 and C_3H_8 from a $CH_4/C_2H_6/C_3H_8$ ternary mixture. Experimental and simulation studies show that tuning metal nodes and pillar ligand lengths not only constructs robust porous structures with extra aromatic groups but also optimizes pore dimensions, thus significantly boosting the separation performance of low-concentration C_2–C_3 hydrocarbons from CH_4. LIFM-265 outperforms its analogues LIFM-263 and LIFM-264 in methane purification efficiency, C_3H_8 capture capacity, and C_2/C_3 retention time, owing to enhanced C–H···π interactions and pore spatial confinement effects. Additionally, LIFM-265 features excellent physicochemical stability, promising for practical separation applications. This work provides valuable insights for designing pillar-layered porous adsorbents for advanced gas adsorption and separation.

4. Experimental section

4.1 General procedure

The standard synthetic protocol involves dissolving the metal nitrate and ligands in a solvent at room temperature in a 20 mL glass vial. The resulting mixture was sealed and placed in a preheated oven at 85 °C for several days, with crystallization occurring under static conditions. After cooling to room temperature in air, the obtained crystals were filtered and repeatedly washed with fresh solvent.

4.2 Synthesis of LIFM-260

$Zn(NO_3)_2\cdot 6H_2O$ (0.27 mmol, 80 mg), 1,4-dicarboxybenzene (0.07 mmol, 11.25 mg), and ligand H_3BTB-Me (0.06 mmol, 26.75 mg) were dissolved in 2 mL DEF; the solution was then heated at 85 °C for 3 days. Colorless, rod-shaped crystals of LIFM-260 were obtained (yield: 57.6 mg, 72% based on metal), which were then repeatedly washed with diethyl ether (ether).

4.3 Synthesis of LIFM-261

$Zn(NO_3)_2\cdot 6H_2O$ (0.10 mmol, 30 mg), $Cd(NO_3)_2\cdot 4H_2O$ (0.12 mmol, 30 mg), and ligand H_3BTB-Me (0.05 mmol, 22 mg) were dissolved in a mixture of 3 mL of DEF and 6 mL of ethanol solvent; the solution was then heated at 85 °C for 4 days. Colorless, rod-shaped crystals of LIFM-261 were obtained (yield: 19.8 mg, 66% based on metal), which were then repeatedly washed with ether.

4.4 Synthesis of LIFM-262

H_3BTB-Me (0.05 mmol, 22 mg), $Zn(NO_3)_2\cdot 6H_2O$ (0.25 mmol, 75 mg), and BPE (0.11 mmol, 18 mg) were dissolved in 5 mL DMAC and 3 mL H_2O; the solution was then heated at 85 °C for 4 days. Colorless crystals of LIFM-262 were obtained (yield: 49.3 mg, 66% based on metal), which were then repeatedly washed with ether.

14138 | J. Mater. Chem. A, 2026, **14**, 14128–14140

This journal is © The Royal Society of Chemistry 2026

4.5 Synthesis of LIFM-263

H$_3$BTB-Me (0.05 mmol, 22 mg), Zn(NO$_3$)$_2$·6H$_2$O (0.25 mmol, 75 mg), and BPY (0.11 mmol, 18 mg) were dissolved in 6 mL DMAC and 2 mL H$_2$O; the solution was then heated at 85 °C for 4 days. Colorless crystals of LIFM-263 were obtained (yield: 52.1 mg, 69% based on metal), which were then repeatedly washed with ether.

4.6 Synthesis of LIFM-264

H$_3$BTB-Me (0.05 mmol, 22 mg), Zn(NO$_3$)$_2$·6H$_2$O (0.10 mmol, 30 mg), Cd(NO$_3$)$_2$·4H$_2$O (0.12 mmol, 35 mg), and BPE (0.11 mmol, 18 mg) were dissolved in 6 mL DMAC and 7 mL H$_2$O; the solution was then heated at 85 °C for 4 days. Colorless crystals of LIFM-264 were obtained (yield: 20.9 mg, 70% based on metal), which were then repeatedly washed with ether.

4.7 Synthesis of LIFM-265

H$_3$BTB-Me (0.05 mmol, 22 mg), Zn(NO$_3$)$_2$·6H$_2$O (0.10 mmol, 30 mg), Cd(NO$_3$)$_2$·4H$_2$O (0.12 mmol, 35 mg), and BPY (0.11 mmol, 18 mg) were dissolved in 8.5 mL DMAC and 3 mL H$_2$O; the solution was then heated at 85 °C for 4 days. Colorless crystals of LIFM-265 were obtained (yield: 21.3 mg, 71% based on metal), which were then repeatedly washed with ether.

Author contributions

Z.-W. W. and C.-Y. S. directed the research projects and supervised the work, as well as contributed to funding acquisition; Y.-N. G. designed and planned the study; Y.-N. G. conducted the experiments and finished formal analysis; the original draft was written by Y.-N. G. and Z.-W. W.; X.-Y. Z., Z.-Q. Z., L. S., X.-H. X., H.-H. S., C.-X. C., J.-J. J., D. F., and H.-Y. C. revised the manuscript and provided valuable suggestions. All authors discussed the results and contributed to the paper.

Conflicts of interest

There are no conflicts to declare.

Data availability

CCDC 2439978, 2439981, 2439991, 2439992, 2439994, and 2439995 contain the supplementary crystallographic data for this paper.[46a–f]

Supplementary information (SI): materials and instrumentation, single crystal X-ray crystallography, PXRD patterns, TGAs, porosity characterization, calculations of Q_{st}, breakthrough experiments, theoretical calculations, Tables S5 and S6, and further experimental details. See DOI: https://doi.org/10.1039/d6ta00133e.

Acknowledgements

References

1 S. Wang, S. Zhu, Y. Jiang, X. Lan, J. Dong, S. Liu, G. Tang, X. He, C. Li, Y. Chen and J. Wang, *Sens. Actuators, B*, 2025, **436**, 137698.

2 X. Zhang, L. Li, J.-X. Wang, H.-M. Wen, R. Krishna, H. Wu, W. Zhou, Z.-N. Chen, B. Li, G. Qian and B. Chen, *J. Am. Chem. Soc.*, 2020, **142**, 633–640.

3 Z. M. Cao, G. L. Li, Z. Y. Di, C. Chen, L. Y. Meng, M. Wu, W. Wang, Z. Zhuo, X. J. Kong, M. Hong and Y. G. Huang, *Angew. Chem., Int. Ed.*, 2022, **61**, e202210012.

4 L.-P. Zhang, Y.-T. Li, Y. Jiang, R.-Y. Jiang, S. Ni and Q.-Y. Yang, *Inorg. Chem. Front.*, 2025, **12**, 3602–3610.

5 S. Chand Pal, R. Krishna and M. C. Das, *Chem. Eng. J.*, 2023, **460**, 141795.

6 R. Sahoo and M. C. Das, *Coord. Chem. Rev.*, 2021, **442**, 213998.

7 Y. Sun, M.-Y. Gao, Y. Sun, D.-F. Lu, F. Wang and J. Zhang, *Inorg. Chem.*, 2021, **60**, 13955–13959.

8 X. Du, D. Pang, Y. Zhao, Z. Hou, H. Wang and Y. Cheng, *Arab. J. Chem.*, 2022, **15**, 103665.

9 X. Huang, F. Chen, H. Sun, W. Xia, Z. Zhang, Q. Yang, Y. Yang, Q. Ren and Z. Bao, *Sep. Purif. Technol.*, 2022, **292**, 121059.

10 J. Wang, W. Fu, L. Wang, Y. Li, Y. Li, Z. Sui and X. Xu, *Chem. Eng. J.*, 2023, **477**, 147128.

11 X. Yuan, S. W. Choi, E. Jang and K. B. Lee, *Chem. Eng. J.*, 2018, **336**, 297–305.

12 Z.-F. Li, Q. Zhang, L.-L. Wang, Y.-L. Li, S.-Q. Yang and T.-L. Hu, *Sep. Purif. Technol.*, 2025, **355**, 129685.

13 K. Adil, Y. Belmabkhout, R. S. Pillai, A. Cadiau, P. M. Bhatt, A. H. Assen, G. Maurin and M. Eddaoudi, *Chem. Soc. Rev.*, 2017, **46**, 3402–3430.

14 T. A. Makal, J.-R. Li, W. Lu and H.-C. Zhou, *Chem. Soc. Rev.*, 2012, **41**, 7761–7779.

15 L. Tang, Q. C. Lin, Z. Jiang, J. Hu, Z. Liu, W. M. Liao, H. Q. Zhou, L. H. Chung, Z. Xu, L. Yu and J. He, *Adv. Funct. Mater.*, 2023, **33**, 2214450.

16 S. M. Wang, M. Shivanna and Q. Y. Yang, *Angew. Chem., Int. Ed.*, 2022, **61**, e202201017.

17 Q.-J. Wu, J. Liang, Y.-B. Huang and R. Cao, *Acc. Chem. Res.*, 2022, **55**, 2978–2997.

18 L. Wang, W. Sun, S. Duttwyler and Y. Zhang, *J. Solid State Chem.*, 2021, **299**, 122167.

19 Z. Zeng, W. Wang, X. Xiong, N. Zhu, Y. Xiong, Z. Wei and J.-J. Jiang, *Inorg. Chem.*, 2021, **60**, 8456–8460.

20 X.-X. Zhang, X.-Z. Guo, S.-S. Chen, H.-W. Kang, Y. Zhao, J.-X. Gao, G.-Z. Xiong and L. Hou, *Chem. Eng. J.*, 2023, **466**, 143170.

This journal is © The Royal Society of Chemistry 2026

J. Mater. Chem. A, 2026, **14**, 14128–14140 | **14139**

21 H.-T. Zheng, L. Song, L. Yan, X.-H. Xiong, Y.-L. Lu, C.-X. Chen, M. Barboiu, Z.-W. Wei, J.-J. Jiang and C.-Y. Su, *Sep. Purif. Technol.*, 2025, **354**, 129466.

22 L. Zhang, X.-H. Xiong, L.-L. Meng, L.-Z. Qin, C.-X. Chen, Z.-W. Wei and C.-Y. Su, *J. Mater. Chem. A*, 2023, **11**, 12902–12909.

23 W. L. Q. Eric, D. Bloch, R. Krishna, J. M. Zadrozny, C. M. Brown and J. R. Long, *Science*, 2012, **335**, 1606–1610.

24 L. Yan, H.-T. Zheng, L. Song, Z.-W. Wei, J.-J. Jiang and C.-Y. Su, *ACS Appl. Mater. Interfaces*, 2024, **16**, 6579–6588.

25 L.-Z. Qin, X.-H. Xiong, S.-H. Wang, L. Zhang, L.-L. Meng, L. Yan, Y.-N. Fan, T.-A. Yan, D.-H. Liu, Z.-W. Wei and C.-Y. Su, *ACS Appl. Mater. Interfaces*, 2022, **14**, 45444–45450.

26 I. Senkovska, V. Bon, L. Abylgazina, M. Mendt, J. Berger, G. Kieslich, P. Petkov, J. Luiz Fiorio, J. O. Joswig, T. Heine, L. Schaper, C. Bachetzky, R. Schmid, R. A. Fischer, A. Pöppl, E. Brunner and S. Kaskel, *Angew. Chem., Int. Ed.*, 2023, **62**, e202218076.

27 T. Li, X. Li, Y. Wang, X. Jia, H. Chen, Y. Li, J. Yang, J. Li and L. Li, *Sep. Purif. Technol.*, 2025, **361**, 131359.

28 G.-D. Wang, R. Krishna, Y.-Z. Li, Y.-Y. Ma, L. Hou, Y.-Y. Wang and Z. Zhu, *ACS Mater. Lett.*, 2023, **5**, 1091–1099.

29 V. Guillerm and M. Eddaoudi, *Acc. Chem. Res.*, 2021, **54**, 3298–3312.

30 D. Song, H. Hou, Y.-J. Gao, F. Jiang, D. Yuan, Q. Chen, L. Liang, D. Wu and M. Hong, *Cryst. Growth Des.*, 2018, **18**, 1826–1833.

31 W. Yuan, P. Guo, W. Wang, P. Cen, X.-Y. Li, B. Liu and H. Zhou, *ACS Mater. Lett.*, 2024, **6**, 3925–3931.

32 M. Li, L. Yin, S. Li, J. Miao, Z. Wang and H. Wang, *Inorg. Chem.*, 2025, **64**, 12440–12445.

33 N. Dutta, G. C. Giri, S. Haldar, G. Vijaykumar, C. D. Stewart, L. Carrella, G. T. Musie and M. Bera, *ChemistrySelect*, 2019, **4**, 10260–10269.

34 V. Machado, M. Turnbull and L. Dawe, *Crystals*, 2018, **8**, 114.

35 A. L. Spek, *J. Appl. Crystallogr.*, 2003, **36**, 7–13.

36 J.-R. Li, R. J. Kuppler and H.-C. Zhou, *Chem. Soc. Rev.*, 2009, **38**, 1477–1504.

37 K. S. Walton and D. S. Sholl, *AIChE J.*, 2015, **61**, 2757–2762.

38 J. L. Rowsell and O. M. Yaghi, *J. Am. Chem. Soc.*, 2006, **128**, 1304–1315.

39 P. Zhang, X. Wen, L. Wang, Y. Zhong, Y. Su, Y. Zhang, J. Wang, J. Yang, Z. Zeng and S. Deng, *Chem. Eng. J.*, 2020, **381**, 122731.

40 P. Huang, C. Chen, F. Jiang, M. Wu and M. Hong, *Cryst. Growth Des.*, 2019, **19**, 3103–3108.

41 D. Wang, T. Zhao, Y. Cao, S. Yao, G. Li, Q. Huo and Y. Liu, *Chem. Commun.*, 2014, **50**, 8648–8650.

42 J. Jia, L. Wang, F. Sun, X. Jing, Z. Bian, L. Gao, R. Krishna and G. Zhu, *Chem.–Eur. J.*, 2014, **20**, 9073–9080.

43 L.-Z. Qin, X.-H. Xiong, S.-H. Wang, L. Zhang, L.-L. Meng, L. Yan, Y.-N. Fan, T.-A. Yan, D.-H. Liu, Z.-W. Wei and C.-Y. Su, *ACS Appl. Mater. Interfaces*, 2022, **14**, 45444–45450.

44 M. Fischer, F. Hoffmann and M. Fröba, *ChemPhysChem*, 2010, **11**, 2220–2229.

45 L. Gong, Y. Ye, Y. Liu, Y. Li, Z. Bao, S. Xiang, Z. Zhang and B. Chen, *ACS Appl. Mater. Interfaces*, 2022, **14**, 19623–19628.

46 (*a*) CCDC 2439978: Experimental Crystal Structure Determination, 2026, DOI: 10.5517/ccdc.csd.cc2mwzzh; (*b*) CCDC 2439981: Experimental Crystal Structure Determination, 2026, DOI: 10.5517/ccdc.csd.cc2mx02n; (*c*) CCDC 2439991: Experimental Crystal Structure Determination, 2026, DOI: 10.5517/ccdc.csd.cc2mx0dz; (*d*) CCDC 2439992: Experimental Crystal Structure Determination, 2026, DOI: 10.5517/ccdc.csd.cc2mx0f0; (*e*) CCDC 2439994: Experimental Crystal Structure Determination, 2026, DOI: 10.5517/ccdc.csd.cc2mx0h2; (*f*) CCDC 2439995: Experimental Crystal Structure Determination, 2026, DOI: 10.5517/ccdc.csd.cc2mx0j3.

14140 | *J. Mater. Chem. A*, 2026, **14**, 14128–14140

This journal is © The Royal Society of Chemistry 2026